ADVANCED MATERIALS TECHNOLOGIES
www.advmattechnol.de

Simultaneously Achieving Ultrahigh Sensitivity and Wide Detection Range for Stretchable Strain Sensors with an Interface-Locking Strategy

Waner Lin, Chubin He, Huayi Huang, Wenyu Zhao, Yanbing Qiu, Xiao Guan, Qi Zhang, Ziya Wang, and Zhengchun Peng**

The development of stretchable strain sensors is crucial for the implementation of electronic skins and wearable electronics. Resistive-type strain sensors are typically composed of an electrically conductive sensing layer coupled to a stretchable substrate. When a sensor is stretched, microstructural changes in the sensing layer lead to a strain-dependent change in resistance. However, strain sensors with high sensitivity and specificity often suffer from a limited detection range along with reliability issues. Here, a novel strain sensor composed of Ag particles and long-range entangled carbon nanotubes (CNTs) with a special composite design is proposed, in which a strain-induced self-locking effect is introduced at the interface between the CNT film and a percolating network consisting of Ag particle filler. As a result, the sensors achieve significantly enhanced performance such as large stretchability (≥120%), high gauge factor (3990.8), fast response time (<33 ms), and high mechanical durability. A range of wearable applications including radial artery, facial expression, and joint motion monitoring are demonstrated, which range from minute deformation to excessive stretching of the sensor.

1. Introduction

Soft wearable electronics are in high demand in various fields, such as health monitoring,[1] human–machine interfaces,[2] and robotics electronic skin.[3] As essential components of soft electronics, stretchable strain sensors have rapidly advanced over the past several years.[4] They are typically used for monitoring multiple physiological functions of human body, including not only large-scale strain (such as bending of the trunk and hand gestures), but also delicate strain (such as breathing and vocal-cord vibration). Hence, it is important that stretchable strain sensors applied in biomechanics, physiology, and kinesiology achieve well-balanced performance. However, due to the dilemma of the percolation principle, it is difficult to develop conductive material-filled elastomer-based strain sensors with both a wide measurement range and high accuracy. For instance, Li et al. reported a graphene strain sensor with a large gauge factor (GF) of over 1000, but its tensile limit was only 3%.[5] Kim et al. reported a strain sensor based on Ag flake/Ag nanocrystal, which realized ≈80% maximum strain, but the GF was just 7.1.[6]

For metal particle-based strain sensors,[7] their sensitivity, response time, and reliability are essentially dependent on the percolation effect between metal particles.[8] The spacing between metal particles that have a low aspect ratio can be readily enlarged during bending or stretching of the substrate, resulting in a rapid decrease in conductivity.[9] Nevertheless, the metal particle-based conductive network can be broken once the particles are separated far enough,[10] leading to the insufficient working range of such devices. Carbon nanotubes (CNTs), a nano-sized fiber with outstanding mechanical properties, high aspect ratio (>100), large Young's modulus, and strong tensile strength, are widely used as a functional material in soft electronics. CNT sensors with random and superimposed percolative networks can bear the large strain; moreover, the chain entanglement and toughness of CNTs make them inherently stable.[11] However, CNT sensors are not suitable for precise perception because of its unsatisfactory sensitivity.[12]

Given these issues, it is difficult for a single functional material to meet the requirements for high sensitivity, large stretchability, and good durability of strain sensors simultaneously, due to the intrinsic features of the material. Therefore, combining synergetic materials is the mainstream approach to enhancing sensing performance. In this work, we developed a stretchable strain sensor with a compositing made of Ag particles and a CNT network. Unlike other hybrid structures reported so far, which showed very limited consideration and engineering at the interface,[8a,12a] this work, for the first time,

W. Lin, C. He, H. Huang, Y. Qiu, X. Guan, Q. Zhang, Prof. Z. Peng
Center for Stretchable Electronics and Nano Sensors
Key Laboratory of Optoelectronic Devices and Systems
of Ministry of Education
College of Optoelectronic Engineering
Shenzhen University
Shenzhen 518060, P. R. China
E-mail: zcpeng@szu.edu.cn
W. Zhao, Dr. Z. Wang
Shenzhen Institute of Artificial Intelligence and Robotics for Society
Shenzhen 518129, P. R. China
E-mail: wzywolf@163.com
The ORCID identification number(s) for the author(s) of this article can be found under https://doi.org/10.1002/admt.202000008.

DOI: 10.1002/admt.202000008

introduces a strain-induced locking mechanism at the interface of the two materials. The interface-locked Ag particles by a CNT network (ILAC) helps build a very stable percolation network with high strength and stretchability. The performance of our strain sensor reveals overall improvement, including an excellent GF (3990.8), sufficiently large strain (≥120%), fast response time (<33 ms), and great durability (≈15 000 cycles without degradation after reaching equilibrium). Thus, the device can accurately measure strain from a delicate deformation to an intense stretch, not only detecting delicate pulse signals and facial expressions, but also hand gestures and joint motions. The experimental results suggest that our sensor has potential applications in health monitoring and human–machine interfaces.

2. Results and Discussion

To avoid low yield and poor uniformity, we employed layer-by-layer deposition of the active components in the fabrication of the ILAC strain sensor (**Figure 1**a). First, an Ag particle solution was dropped on a clean glass substrate, which was covered by a polymeric template (hollow mask) with a specifically designed pattern. Next, a homogeneous dispersed CNT solution was sprayed on top of the Ag particle solution to form a contiguous CNT film. After drying, a two-tier percolative network was formed, and the polymer mask removed. Then a polydimethylsiloxane (PDMS) precursor was poured onto the glass substrate to fully embed the CNT film and the Ag particles. Finally, the cured elastomer with the integrated conductive network was peeled off the glass substrate without any Ag particles or CNTs remaining. Figure 1b shows photographs of a representative ILAC device, which can be readily twisted, bent, and stretched without any structural damage or electrical disconnection (strain–stress curves are shown in Figure S1, Supporting Information).

To optimize the concentrations of the Ag particle and CNT dispersion for the best electromechanical performance of the ILAC sensor, strain sensors made of pure Ag particle networks with various concentrations of Ag particle solution were first fabricated. Figure 1c,d shows that the relative resistance change in pure Ag devices under stretching becomes smaller, and eventually insensitive, with increasing Ag concentration. The sensor made with the lowest Ag particle concentration (0.03 g mL^{-1})

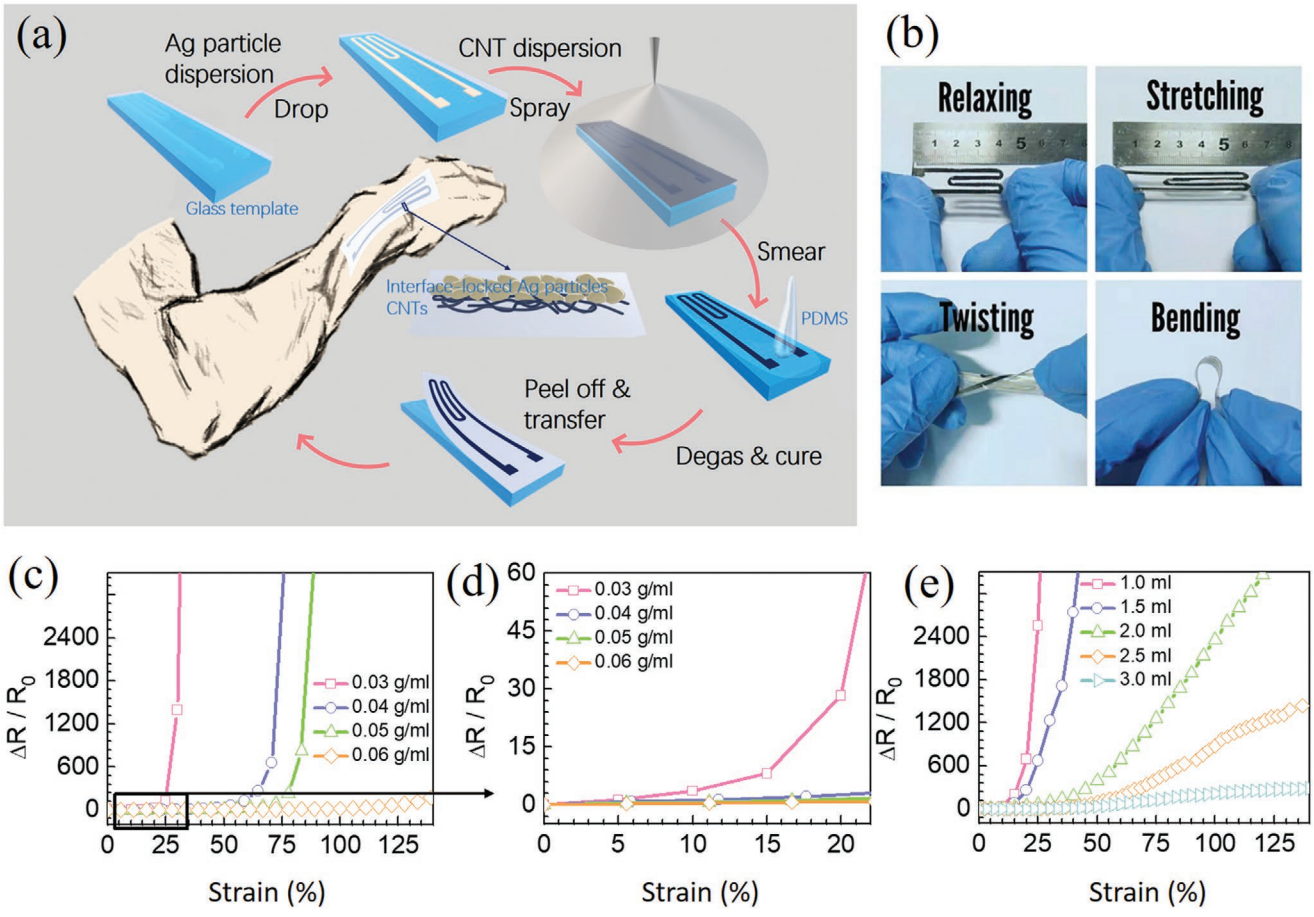

Figure 1. Schematic of the fabrication process flow of the ILAC sensor and the optimization of the ingredients. a) Fabrication process flow of the ILAC sensor. b) Photograph of the ILAC sensor in relaxing, stretching, twisting, and bending states. c,d) Relative resistance change of a strain sensor made of pure Ag particle network as a function of Ag particle concentration. e) Relative resistance change of the ILAC sensor at Ag concentration of 0.03 g mL^{-1} with various volumes of CNT dispersion.

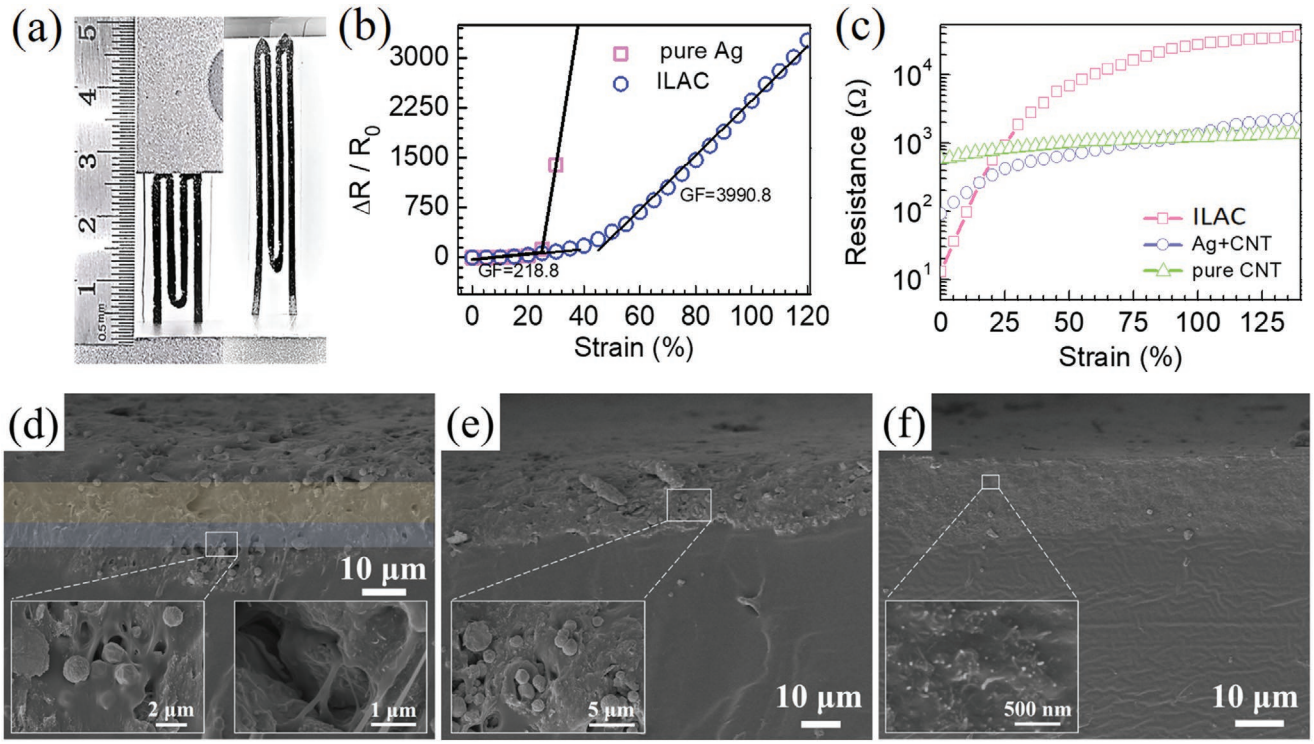

Figure 2. a) Photographs of the ILAC sensor being stretched to the strain of 100%. b) Relative resistance change of the pure Ag sensor and the ILAC sensor as a function of strain. c) Resistance response of three different types of strain sensors. Cross-section view SEM images of d) ILAC, e) Ag+CNT, and f) pure CNT sensors.

can readily induce percolative fragmentation, resulting in the highest sensitivity to strain. However, the device fails electrically at just about 25% strain. Such a strain sensor is incompetent for monitoring large motions, such as limb bending and torsion.[13] Therefore, it is necessary to introduce a second phase material, and ensure it produces a synergetic effect with the Ag particle network to enable a highly stretchable sensor.[14] Therefore, we propose a way to achieve multiple, longer pathways of electrical connection among Ag particles by spray-coating a CNT dispersion on top of the Ag particle solution (0.03 g mL^{-1}). As shown in Figure 1e, a thicker CNT coating significantly extends the efficacy range of the strain sensor, while reducing its sensitivity. Taking into consideration the requirement of stretchability up to 100% (**Figure 2**a) for joint-mounted wearable devices and a relatively high sensitivity, the ILAC sensor consisting of 2 mL of CNT dispersion (5 mg mL^{-1}) is the optimal solution for a variety of strain-sensing applications.

The electromechanical performance of the pure Ag sensor and that of the ILAC sensor are compared in Figure 2b, for which the GFs of the sensors were calculated by the following equation:[15]

$$\mathrm{GF} = \frac{\Delta R/R_0}{\varepsilon} = \frac{(R - R_0)/R_0}{\varepsilon} \quad (1)$$

where ε is the mechanical strain applied to the sensor, R_0 is the initial resistance at $\varepsilon = 0\%$, and R is the resistance at an applied strain. Although the pure Ag sensor exhibits a decent GF of 218.8, its percolation threshold is only about 25% strain. On the contrary, the strain-sensing range of ILAC is extended beyond 120%. The GF reaches an impressively high value of 3990.8 with excellent linearity under a strain greater than 40%. These results are superior to those obtained for most stretchable strain sensors reported so far.[3b,5,6,16] Interestingly, the ILAC sensor exhibits a GF almost identical to that of the pure Ag sensor in the low strain range of $\varepsilon < 25\%$. This means that under low strain, the interaction between Ag particles contributes greatly to the change in the resistance of the ILAC sensor.

In order to verify the advantages of the ILAC sensor, we prepared two control samples. One was made from a pure CNT solution, and the other was made from a well-mixed Ag particle and CNT solution (Ag+CNT). For both samples, we employed the same design and similar fabrication processes as those used for the ILAC sensor. Figure 2c shows the relative resistance changes in the ILAC sensor and the two reference sensors during stretching. All three sensors could be stretched up to 120%. However, the ILAC sensor exhibited a much higher sensitivity (GF = 3990.8), while the Ag+CNT sensor and the pure CNT sensor showed a dramatically decreased sensitivity to strain with GFs of 160.9 and 56.4, respectively. This can be attributed to the intrinsically stable resistance of the "bulky" CNT network to strain. In addition, the ILAC sensor demonstrated a much larger linearity range under low strain than the Ag+CNT sensor, and a much lower initial resistance (<10 Ω) than the pure CNT sensor.

To analyze the microstructure of the two-tier percolative network, the cross-section morphology of the ILAC, Ag+CNT, and pure CNT sensors were characterized by scanning electron

microscopy (SEM). Figure S2, Supporting Information, shows that homogeneous Ag particles of about 2 µm were densely embedded in the PDMS elastomer matrix, leading to a continuous conductive pathway. For the sample with 0.03 g mL^{-1} Ag concentration, the average thickness of the Ag particle network was about 10 µm. The sheet resistance was about 9.9 Ω cm^{-2}. A lower concentration of Ag would lead to insufficient conductivity, while an excessive concentration of Ag would result in a seriously deteriorated response to strains. After coating a 2 mL CNT dispersion (5 mg mL^{-1}), we observed that the CNTs were mainly distributed between the Ag particle network and the PDMS substrate (Figure 2d). The thickness of the CNT layer was about 5 µm. It is worth noting that the CNT network partially filled the void space among Ag particles at the interface and helped build multiple longer pathways of electrical connection among Ag particles. In comparison, the CNT network of the Ag+CNT sensor (Figure 2e) could not effectively act on the neighboring Ag particles. However, the sizes and surface properties mismatches between Ag particles and CNTs led to the local stacking of CNT networks, resulting in dramatically reduced sensitivity of the strain sensor. Figure 2f shows the cross-sectional morphology of pure CNTs/PDMS. Above all, no debonding or cracks between the conductive network/PDMS layer and the PDMS body was observed when the transfer-printing method was used.

Based on the above findings, we propose a novel interface-locked mechanism to explain the excellent performances of the ILAC sensor. **Figure 3**a–c presents schematic diagram of tracking microstructural evolution during stretching. In the initial state, the conductive compounds composed of laminated Ag particles and CNTs construct an integrated conductive percolation network. The electron channels of the sensor are mainly contributed to by the interconnected Ag particles because the conductivity of Ag is orders of magnitude higher than that of CNTs (Figure 3a). Under small stretching, parts of the conductive paths were cut off by the separation between Ag particles due to the weak interfacial binding and large mechanical mismatch between the conductive particles and the polymer matrix,[15] resulting in increased electrical resistance (Figure 3b, corresponding to zone I of Figure 3d). On the other hand, under the action of transverse Poisson compression during stretching, inter-particle slippage between Ag particles and CNTs took place, which induced nanopile interlocking in the boundary. Under a large strain (>40%), the original conductive paths of Ag particles were fully destroyed, as in the pure Ag sensor previously reported studies (Figure 3c, corresponding to zone II of Figure 3d).[16,17] Figure 3e shows the microscopic behavior of the ILAC component PDMS film with various tensile strains. We demonstrated that interface-locked Ag particles (yellow areas) gradually emerge in the CNT network (black areas) during stretching. However, thanks to the special Ag-CNT sensing layer formed in the interface region, where the long-range connective CNT network interlocks the Ag particles and keeps them at an appropriate interaction distance, the device maintains the efficient resistance response over a large strain range. CNTs prevent the separation of Ag particles like the sand fixation plants. At this point, the special Ag-CNT sensing layer constitutes the main electronic channels. It is different from the preceding Ag+CNT sample, in which the Ag conductive paths were almost blocked by hybrid CNTs, leading to the high initial resistance and small GF (Figure 3f).

Considering various applications where the appropriate size and parameter are desired, we studied the influence of various patterns on the electromechanical properties. As seen in Figure S3, Supporting Information, a great number of channels can improve the sensitivity of the ILAC sensor in the longitudinal

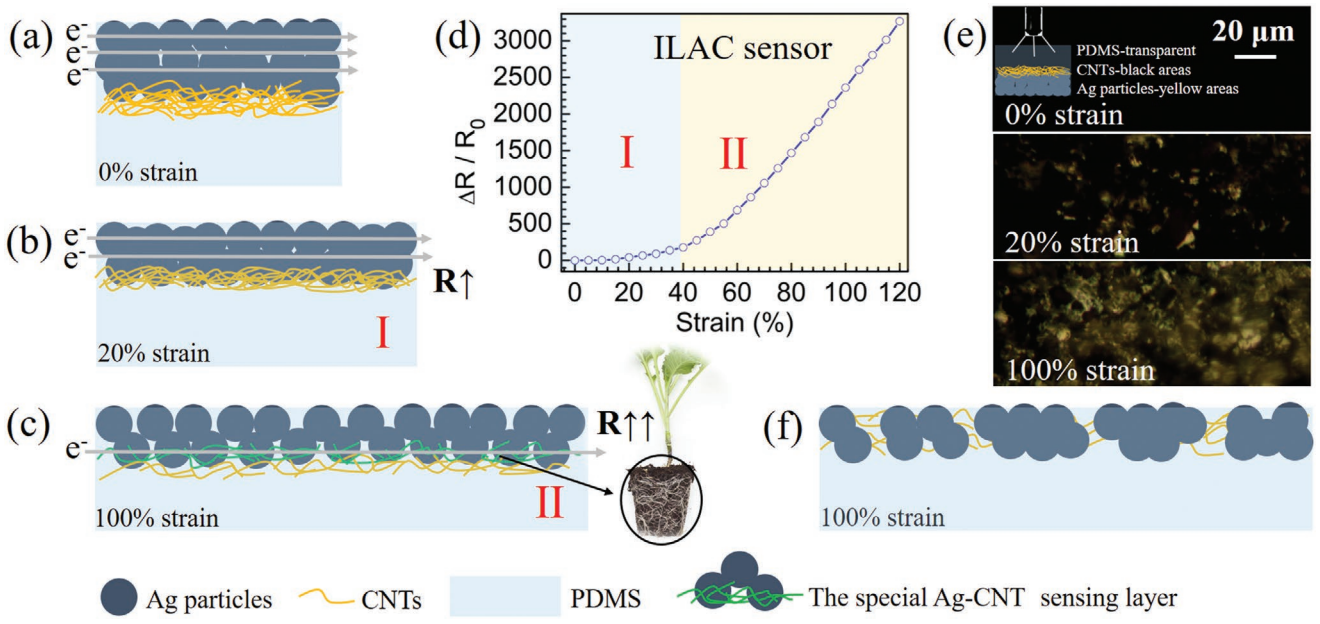

Figure 3. The proposed sensing mechanism in the ILAC sensor. Schematic illustrations of ILAC sensor corresponding to a) initial state, b) 20% strain, and C) 100% strain. d) Relative resistance change versus stain of the ILAC sensor. e) Representative optical microscopy images during stretching. f) Schematic illustrations of Ag+CNT sensor under 100% strain.

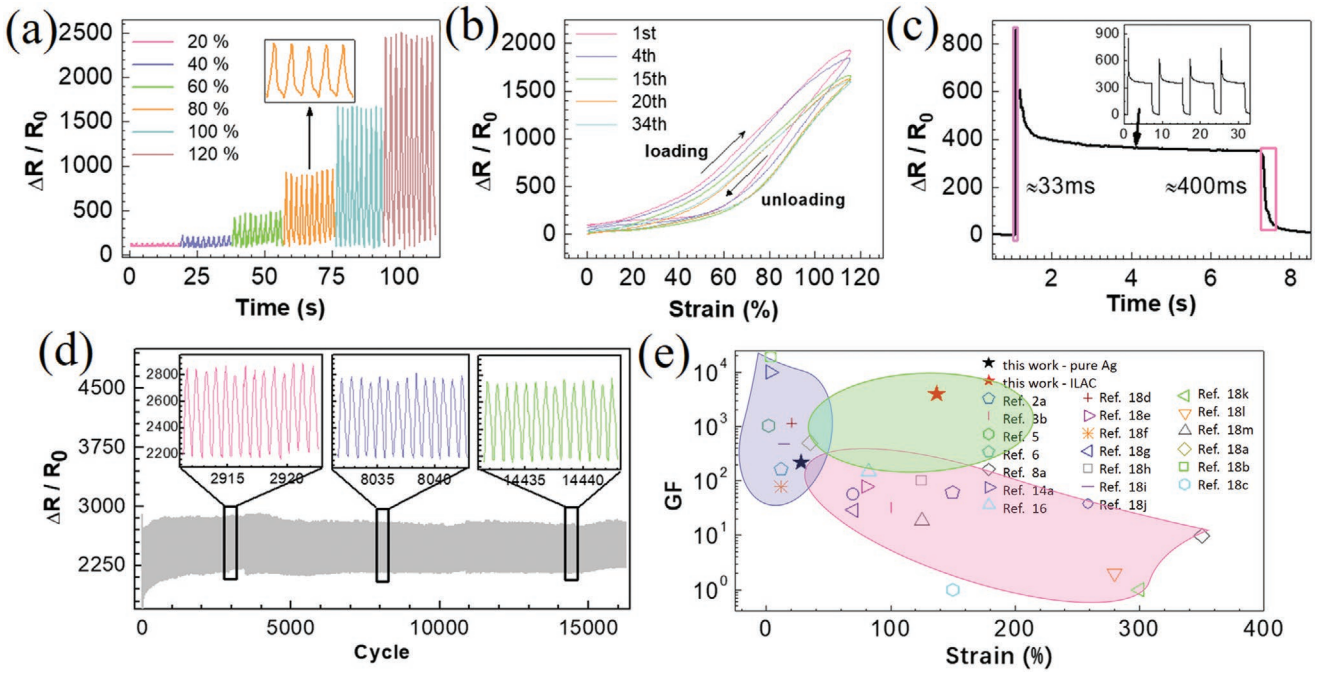

Figure 4. Electromechanical performances of patterned ILAC sensor. a) Step responses of the ILAC sensor under strain ranging from 20% to 120%. b) The $\Delta R/R_0$ curves of the 1st, 4th, 15th, 20th, and 34th cycles of the ILAC sensor under the strain of 120% at the stretching rate of 0.1 Hz. c) Response time of the ILAC sensor under the tensile strain of 60% (10 m s^{-1}). d) The resistance response of the ILAC sensor during 15 000 loading–unloading cycles with 120% strain at a rate of 1.75 Hz. e) Comparison of the GF versus strain for previously reported stretchable strain sensors.

direction and minimize the signal response from transverse loading. For the patterned ILAC device (2 strips), **Figure 4**a shows the resistance responses, which changed with time under the various applied strains ranging from 20% to 120%. It can be observed that resistance repeatedly changed with strain loading–unloading. Moreover, the stability and consistency of signals for applied strain are demonstrated by the zoomed-in waves in Figure 4a and Figure S4, Supporting Information. The hysteresis behavior of the ILAC sensor was examined by a series of cyclic 120% stretching. The $\Delta R/R_0$ curves of the 1st, 4th, 15th, 20th, and 34th cycles were selected and depicted in Figure 4b. Despite the unstable hysteresis, overall, the ILAC sensor maintained a low threshold (<20%) owing to the firm interface-locked strain-sensing system. Based on the proposed interface-locked mechanism in the ILAC sensor, transverse compression continuously decreases the contact resistance of the Ag particle and CNT interface under stretching. Although ILAC sensor showed about 10% resistance reduction between the 1st and 34th cycles, the resistance change is diminished in subsequent cycles. To evaluate the response time of the ILAC sensor, a dynamic tensile strain of 60% was applied. The device shows the fast response time of less than 33 ms, which demonstrates that the ILAC sensor has adequate ability to detect strain responses in real-time (Figure 4c). However, unsatisfactory releasing time (≈400 ms) is mainly due to the viscoelasticity and hysteresis of PDMS.[10,13] The durability of the ILAC sensor was measured by repetitive loading–unloading cycles (120% strain) with more than 15 000 cycles at a frequency of 1.75 Hz (Figure 4d). The sudden increase in the resistance change at the initial state can be attributed to the inertia of the overload stretch/release during the dynamic measurement and the irreversible inter-particle slippage between the Ag particles and CNTs during the initial stretch cycles. As the test continues, the contact resistance between the Ag particle and CNT layer continues to decrease about 10% from the 2000th cycle to the end of test (≈15 000th cycle). This phenomenon is attributed to the stretching-induced nanopile interlocking process. Figure 4e summarizes the key parameters of the ILAC sensor compared with those of other stretchable strain sensors reported recently.[2a,3b,5,6,8a,14a,16,18] It can be seen that there is generally a compromise between the sensitivity and measurement range. Sensors with ultrahigh sensitivity tend to show a narrow effective range; to achieve a wide measurement range, there must be a sacrifice of sensitivity. In contrast, the ILAC sensor with a competitively short response time and high durability allows decoupled tuning of the electrical and mechanical properties, thus ensuring an excellent sensitivity and measurement range simultaneously. This interface-locked state of the CNT network for conductive Ag particles is considered the main reason for the increased effective measurement range of the pure Ag sensor.

Benefiting from its excellent sensitivity and measurement range, the ILAC sensor shows tremendous potential for applications in wearable human activity detection under a large strain (>100%) and bending angle (≈150°). **Figure 5** shows the capability of the ILAC sensor for the monitoring of intense human motion. To monitor hand gesture patterns, five individual ILAC sensors were applied to a data glove. Figure 5a shows the differential resistance variation with the gradually increased bending angles of the subject's finger. In the bending cycles, the ILAC sensor exhibited favorable sensitivity and reproducibility. Furthermore, as shown in Figure 5b, the real-time motions of the

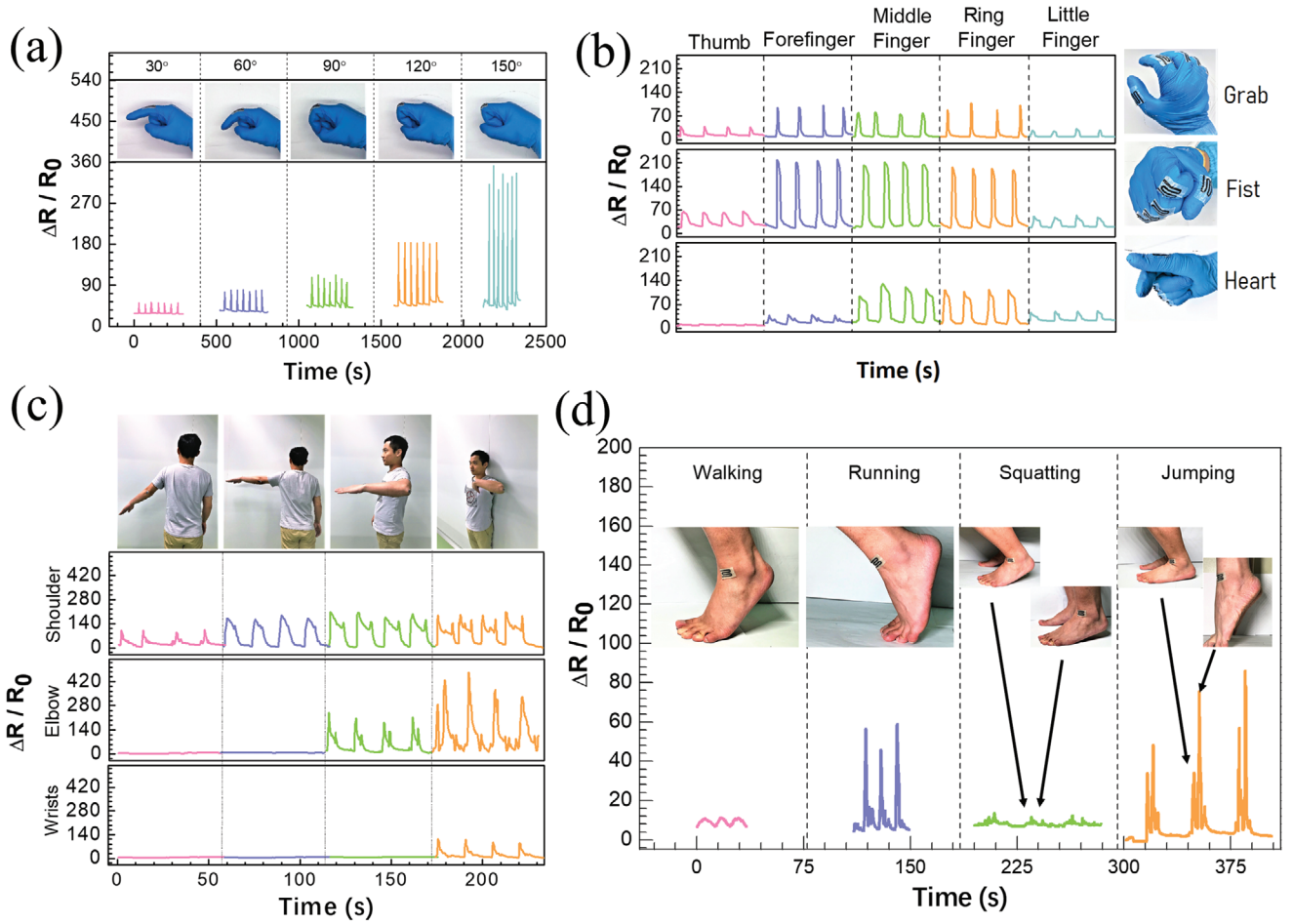

Figure 5. a) Sensing performance of the ILAC sensor on finger bending. b) Real-time monitoring for gesture recognition. c) Real-time monitoring for bending motion of upper limb. d) Real-time monitoring for the ankle joint under exercise. Insets show the corresponding photographic images.

fingers (such as making a fist, and a heart shape) were precisely tracked by monitoring the relative resistance response of the ILAC sensors. The ILAC sensors could also be integrated into the body guards to distinguish large-scale movement of joints. To detect the motions of the upper limb, three devices were respectively applied to the shoulder, elbow, and wrist of a subject. Figure 5c shows the obtained regular resistance responses when the subject raised his arm and bent his elbow and wrist, respectively. Similarly, motions of the ankles (walking, running, squatting, and jumping) were recorded (Figure 5d). All the electronic signals can easily be attributed one-to-one to specific actions based on differentiating frequency, resistance changes, and curve patterns. Therefore, a bionic mannequin for real-time motion capture was generated in the virtual environment with the assistance of LabVIEW and displayed in the Movie S1, Supporting Information.

On the other hand, the ILAC sensors were attached on the wrist and face to recognize small-scale strain ($\varepsilon \leq 5\%$), such as the pulse and facial expressions. **Figure 6**a shows the real-time pulse signals of the radial artery recorded by the ILAC device. The pulse is a significant physiological signal that reflects systolic and diastolic ventricle activity as well as the heart rate. The typical characteristics of a pulse waveform, including the percussion wave, tidal wave, and diastolic wave can be promptly and accurately observed (Figure 6b).[8a,19] Obviously, the ILAC strain device was sensitive enough to describe the typical pulse waveform in relaxation (80 beats min^{-1}), in contrast to the irregular shape after exercise (122 beats min^{-1}). In addition, four devices were placed on each side of the mouth and forehead for recognizing various facial expressions. As seen in Figure 6c, the resistance change induced by the stretching of internal muscles in the face were precisely recorded. For example, distinguishing smiling with motion on both side of mouth motion and the funny with only left side of muscle variation. According to these findings, a multichannel sensing and dynamic controlling device for emotion recognition was developed and demonstrated (Movie S2, Supporting Information), verifying the feasibility of applying the ILAC sensor in human–computer interactive systems.

3. Conclusion

In summary, based on the ILAC design, we developed a facile, cost-effective, and scalable approach for preparing a highly stretchable (≥120% strain) and highly sensitive (GF = 3990.8) strain sensor. The mechanism of interface-locked Ag particles

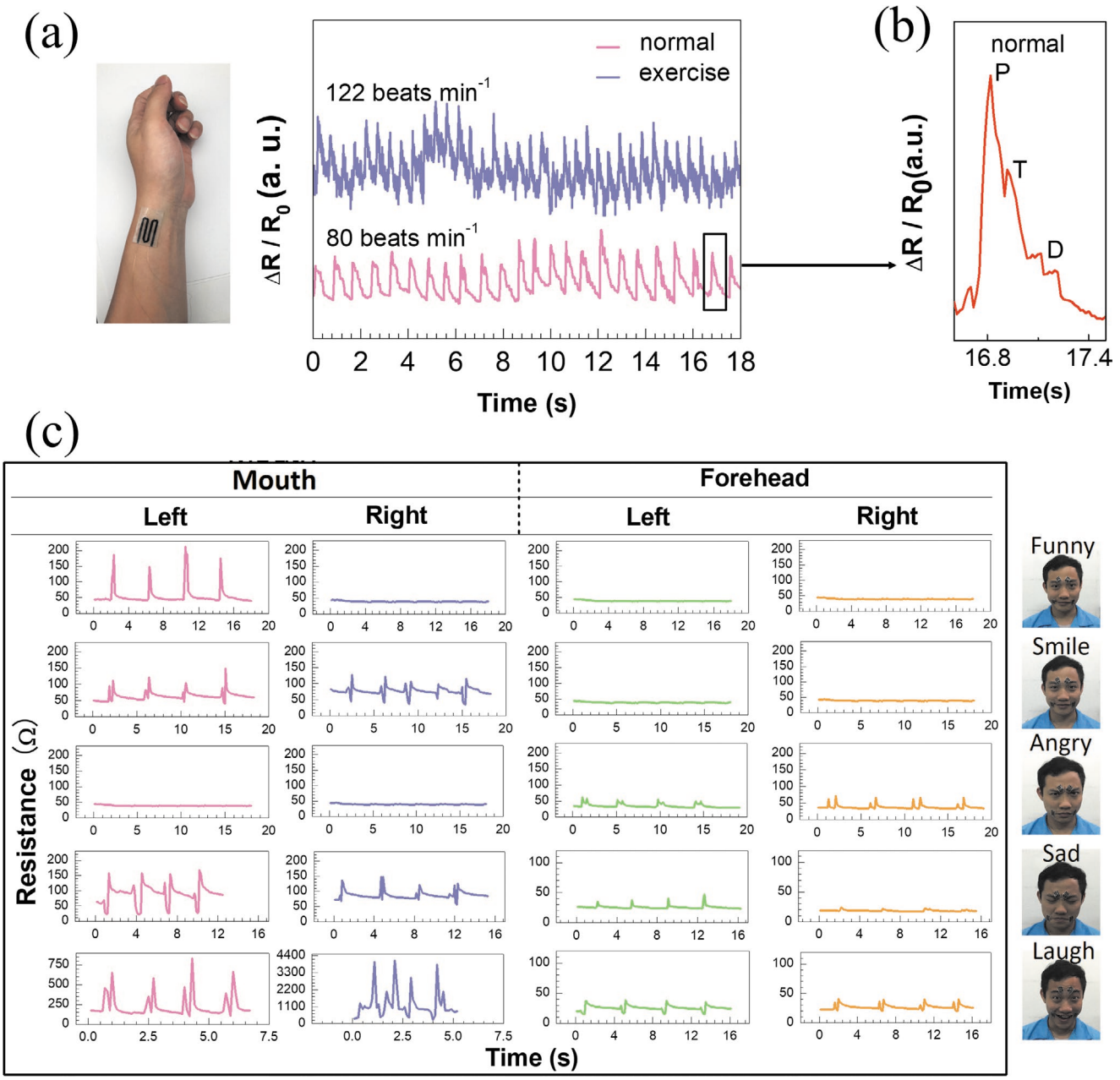

Figure 6. a) Pulse signals recorded by the ILAC sensor. b) The typical pulse waveform in relaxation, in contrast to the irregular shape after exercise. c) Resistance change induced by the stretching of internal muscles in the face, such as funny, smiling, angry, sad, and laughing.

by a CNT network (ILAC) was proposed for the first time; it explains the synergetic effect of both the large measurement range and extraordinary sensitivity. The ILAC sensor also shows fast response speed (<33 ms) and qualified durability over more than 15 000 stretching cycles. Our sensor can accurately measure strain from a delicate deformation to an intense stretch, as demonstrated by pulse detection, facial expression and hand gesture recognition, as well as joint movement monitoring. Therefore, we believe the ILAC sensor has potential for use in a number of applications including wearable electronics for human health monitoring and motion tracking, as well as data gloves for human–machine interface and collaboration.

4. Experimental Section

Materials and Preparation: Commercial Ag micro-particles (Aladdin) were over 99.95 wt% and the particle size was about 2 µm. They were dispersed in alcohol with the concentration ranging from 0.01 to 0.06 g mL^{-1} and sonicated for 30 min. Functionalized multiwall CNTs were purchased from Timesnano with over 98 wt% purity (10–30 µm length, <8 nm outer diameter). To achieve uniformity, a CNT/*n*-hexane dispersion (5 mg mL^{-1}) was prepared by sonication for 3 h.

Fabrication: The Ag particles were deposited on a clean glass substrate with design pattern from alcohol dispersion by dropping method. The specimens were then dried at 80 °C for 5 min to remove the alcohol. Subsequently, the CNT dispersion was spray cast and evaporated at room temperature. The thickness of the CNTs was

dependent on the volume of the CNT/*n*-hexane solution. After drying, the pattern was removed and PDMS (10:1 ratio of the base and curing agent, Sylgard 184, Dow Corning) was poured onto the film. For encapsulation, the films were placed in a vacuum chamber for 20 min, followed by curing at 80 °C for 1 h.

Performance Characterization: The structures of the pure Ag, pure CNT, Ag+CNT, and ILAC strain sensors were characterized by FESEM (Supra 55, ZEISS). The loading of tensile strain was performed with a testing machine (E1000, Instron) which could provide uniform stretching and releasing cycles, while the electrical signals of the strain sensors were recorded at a same time by a digital multimeter (34465A, Keysight).

Detection and Reconstruction of Human Body Motion: To demonstrate the ability for real-time monitoring of human body motions, the ILAC sensors were attached to various joints of the human body, such as the fingers, wrist, elbow, shoulder, face, and so on, using commercial medical adhesive tapes. An avatar face and body were developed in LabVIEW and connected to an integrated test system. The experiments involving human subject have been performed with the full, informed consent of the volunteer in accordance with all local laws and with the approval of all relevant ethics bodies.

Supporting Information

Supporting Information is available from the Wiley Online Library or from the author.

Acknowledgements

This work was supported by the Science and Technology Innovation Commission of Shenzhen (KQTD20170810105439418, JCYJ20170818091233245), the National Natural Science Foundation of China (61903317, 61671308, U1613212), the Natural Science Foundation of Guangdong Province (2018A030310551), the Department of Education of Guangdong Province (2016KZDXM005), the Science and Technology Innovation Council of Shenzhen (JCYJ20170818091233245), and funding from Shenzhen Institute of Artificial Intelligence and Robotics for Society.

Conflict of Interest

The authors declare no conflict of interest.

Keywords

health monitoring, human–machine interaction, interface-locked Ag particles, carbon nanotubes, stretchable strain sensors

Received: January 3, 2020
Revised: February 27, 2020
Published online: April 2, 2020

[1] a) Y. Liu, M. Pharr, G. A. Salvatore, *ACS Nano* **2017**, *11*, 9614; b) T. Q. Trung, N. E. Lee, *Adv. Mater.* **2016**, *28*, 4338; c) I. Kim, K. Woo, Z. Zhong, P. Ko, Y. Jang, M. Jung, J. Jo, S. Kwon, S. H. Lee, S. Lee, H. Youn, J. Moon, *Nanoscale* **2018**, *10*, 7890.

[2] a) S. Gong, D. T. H. Lai, Y. Wang, L. W. Yap, K. J. Si, Q. Shi, N. N. Jason, T. Sridhar, H. Uddin, W. Cheng, *ACS Appl. Mater. Interfaces* **2015**, *7*, 19700; b) X. Liao, Q. Liao, X. Yan, Q. Liang, H. Si, M. Li, H. Wu, S. Cao, Y. Zhang, *Adv. Funct. Mater.* **2015**, *25*, 2395.

[3] a) C. Pang, J. H. Koo, A. Nguyen, J. M. Caves, M. G. Kim, A. Chortos, K. Kim, P. J. Wang, J. B. H. Tok, Z. Bao, *Adv. Mater.* **2015**, *27*, 634; b) Z. Lei, P. Wu, *Nat. Commun.* **2018**, *9*, 1134; c) X. Wang, Y. Gu, Z. Xiong, Z. Cui, T. Zhang, *Adv. Mater.* **2014**, *26*, 1336.

[4] a) D. Chen, Q. Pei, *Chem. Rev.* **2017**, *117*, 11239; b) Y. S. Rim, S. H. Bae, H. Chen, N. de Marco, Y. Yang, *Adv. Mater.* **2016**, *28*, 4415.

[5] X. Li, T. Yang, Y. Yang, J. Zhu, L. Li, F. E. Alam, X. Li, K. Wang, H. Cheng, C. T. Lin, Y. Fang, H. Zhu, *Adv. Funct. Mater.* **2016**, *26*, 1322.

[6] G. Shi, Z. Zhao, J.-H. Pai, I. Lee, L. Zhang, C. Stevenson, K. Ishara, R. Zhang, H. Zhu, J. Ma, *Adv. Funct. Mater.* **2016**, *26*, 7614.

[7] a) Z. Yang, D. Y. Wang, Y. Pang, Y. X. Li, Q. Wang, T. Y. Zhang, J. B. Wang, X. Liu, Y. Y. Yang, J. M. Jian, M. Q. Jian, Y. Y. Zhang, Y. Yang, T. L. Ren, *ACS Appl. Mater. Interfaces* **2018**, *10*, 3948; b) Q. Zhang, L. Liu, D. Zhao, Q. Duan, J. Ji, A. Jian, W. Zhang, S. Sang, *Nanomaterials* **2017**, *7*, 424; c) S. Zhang, L. Cai, W. Li, J. Miao, T. Wang, J. Yeom, N. Sepúlveda, C. Wang, *Adv. Electron. Mater.* **2017**, *3*, 1700067; d) D. J. Kim, D. Ha, Q. Zhou, A. K. Thokchom, J. W. Lim, J. Lee, J. G. Park, T. Kim, *Nanoscale* **2017**, *9*, 9622; e) H. Zhang, N. Liu, Y. Shi, W. Liu, Y. Yue, S. Wang, Y. Ma, L. Wen, L. Li, F. Long, Z. Zou, Y. Gao, *ACS Appl. Mater. Interfaces* **2016**, *8*, 22374.

[8] a) T. Yamada, Y. Hayamizu, Y. Yamamoto, Y. Yomogida, A. Izadi-Najafabadi, D. N. Futaba, K. Hata, *Nat. Nanotechnol.* **2011**, *6*, 296; b) D. J. Cohen, D. Mitra, K. Peterson, M. M. Maharbiz, *Nano Lett.* **2012**, *12*, 1821.

[9] S. Zhao, J. Li, D. Cao, Y. Gao, W. Huang, G. Zhang, R. Sun, C. P. Wong, *J. Mater. Chem. C* **2016**, *4*, 6666.

[10] B. Liang, Z. Lin, W. Chen, Z. He, J. Zhong, H. Zhu, Z. Tang, X. Gui, *Nanoscale* **2018**, *10*, 13599.

[11] a) Y. Jiang, Y. Wang, Y. K. Mishra, R. Adelung, Y. Yang, *Adv. Mater. Technol.* **2018**, *3*, 1800248; b) P. Cataldi, S. Dussoni, L. Ceseracciu, M. Maggiali, L. Natale, G. Metta, A. Athanassiou, I. S. Bayer, *Adv. Sci.* **2018**, *5*, 1700587.

[12] a) H. Zhu, X. Wang, J. Liang, H. Lv, H. Tong, L. Ma, Y. Hu, G. Zhu, T. Zhang, Z. Tie, Z. Liu, Q. Li, L. Chen, J. Liu, Z. Jin, *Adv. Funct. Mater.* **2017**, *27*, 1606604; b) S. Y. Kim, S. Park, H. W. Park, D. H. Park, Y. Jeong, D. H. Kim, *Adv. Mater.* **2015**, *27*, 4178.

[13] S. Han, C. Liu, H. Xu, D. Yao, K. Yan, H. Zheng, H. J. Chen, X. Gui, S. Chu, C. Liu, *npj Flexible Electron.* **2018**, *2*, 16.

[14] a) L. Cai, L. Song, P. Luan, Q. Zhang, N. Zhang, Q. Gao, D. Zhao, X. Zhang, M. Tu, F. Yang, W. Zhou, Q. Fan, J. Luo, W. Zhou, P. M. Ajayan, S. Xie, *Sci. Rep.* **2013**, *3*, 3048; b) J. Lee, M. Lim, J. Yoon, M. S. Kim, B. Choi, D. M. Kim, D. H. Kim, I. Park, S. J. Choi, *ACS Appl. Mater. Interfaces* **2017**, *9*, 26279.

[15] M. Amjadi, K. U. Kyung, I. Park, M. Sitti, *Adv. Funct. Mater.* **2016**, *26*, 1678.

[16] Q. Liu, J. Chen, Y. Li, G. Shi, *ACS Nano* **2016**, *10*, 7901.

[17] K. K. Kim, S. Hong, H. M. Cho, J. Lee, Y. D. Suh, J. Ham, S. H. Ko, *Nano Lett.* **2015**, *15*, 5240.

[18] a) S. Wan, Z. Zhu, K. Yin, S. Su, H. Bi, T. Xu, H. Zhang, Z. Shi, L. He, L. Sun, *Small Methods* **2018**, *2*, 1700374; b) Y. F. Yang, L. Q. Tao, Y. Pang, H. Tian, Z. Y. Ju, X. M. Wu, Y. Yang, T. L. Ren, *Nanoscale* **2018**, *10*, 11524; c) L. Pan, G. Liu, W. Shi, J. Shang, W. R. Leow, Y. Liu, Y. Jiang, S. Li, X. Chen, R. W. Li, *Nat. Commun.* **2018**, *9*, 3813; d) B. Park, J. Kim, D. Kang, C. Jeong, K. S. Kim, J. U. Kim, P. J. Yoo, T. -i. Kim, *Adv. Mater.* **2016**, *28*, 8130; e) X. Liao, Z. Zhang, Q. Liao, Q. Liang, Y. Ou, M. Xu, M. Li, G. Zhang, Y. Zhang, *Nanoscale* **2016**, *8*, 13025; f) T. Yan, Z. Wang, Z. J. Pan, *J. Mater. Sci.* **2018**, *53*, 11917; g) Y. R. Jeong, H. Park, S. W. Jin, S. Y. Hong, S. S. Lee, J. S. Ha, *Adv. Funct. Mater.* **2015**, *25*, 4228; h) Z. Liu, D. Qi, G. Hu, H. Wang, Y. Jiang, G. Chen, Y. Luo, X. J. Loh, B. Liedberg, X. Chen, *Adv. Mater.* **2018**, *30*, 1704229; i) Y. Jiang, Z. Liu, N. Matsuhisa, D. Qi, W. R. Leow, H. Yang, J. Yu, G. Chen, Y. Liu, C. Wan, Z. Liu, X. Chen, *Adv. Mater.* **2018**, *30*, 1706589; j) J. Oh, J. C. Yang, J. O. Kim, H. Park, S. Y. Kwon, S. Lee, J. Y. Sim, H. W. Oh, J. Kim, S. Park, *ACS Nano* **2018**, *12*, 7546; k) J. Lee, S. Shin, S. Lee, J. Song, S. Kang, H. Han, S. Kim, S. Kim, J. Seo, D. Kim, T. Lee, *ACS Nano* **2018**, *12*, 9634; l) U. H. Shin, D. W. Jeong, S. M. Park, S. H. Kim, H. W. Lee, J. M. Kim, *Carbon* **2014**, *80*, 396; m) M. Amjadi, M. Turan, C. P. Clementson, M. Sitti, *ACS Appl. Mater. Interfaces* **2016**, *8*, 5618.

[19] J. S. Heo, J. Eom, Y. H. Kim, S. K. Park, *Small* **2018**, *14*, 1703034.